

Impact parameter manipulation in exclusive photoproduction in Electron-Ion Collisions*

Xin Wu,¹ Xin-Bai Li,¹ Ze-Bo Tang,¹ Kai-Yang Wang,¹ and Wang-Mei Zha^{1,†}

¹*State Key Laboratory of Particle Detection and Electronics,
University of Science and Technology of China, Hefei 230026, China*

In the context of future electron-ion collision experiments, particularly the Electron-Ion Collider (EIC) and the Electron-Ion Collider in China (EicC), investigating exclusive photoproduction processes is of paramount importance. These processes offer a distinctive opportunity to probe the gluon structure of nuclei across a broad range of Bjorken- x , thereby enabling measurements of nuclear shadowing and facilitating the search for gluon saturation and color glass condensates. This study explores the potential of utilizing neutron tagging via the Coulomb excitation of nuclei to precisely determine the impact parameter for exclusive photoproduction in electron-ion collisions. By developing the Equivalent Photon Approximation (EPA) for fast electrons, this study incorporates a coordinate-space-dependent photon flux distribution to elucidate the relationship between the photon transverse momentum distribution and the collision impact parameter. Furthermore, the differential cross section for Coulomb excitation of nuclei is derived by leveraging the spatial information from the photon flux. Our calculations demonstrate that neutron tagging can significantly alter the impact parameter distributions, thereby providing a robust method for impact parameter manipulation in electron-ion collisions. This study provides valuable insights and strategies for exploring the impact parameter dependence of exclusive photoproduction, offering novel insights for experimental design and data analysis. Ultimately, it enhances our understanding of the gluon distribution within the nucleus.

Keywords: Electron-Ion collisions, Exclusive photoproduction, Coulomb dissociation, Gluon tomography

I. INTRODUCTION

Electron-ion collisions present an unparalleled opportunity for investigating the internal structures of nucleons and nuclei [1], particularly the distribution of gluons across different momentum scales. Upcoming facilities, including the Electron-Ion Collider (EIC) [2] in the United States and the Electron-Ion Collider in China (EicC) [3], are specifically designed to probe these structures over a broad range of photon virtuality (Q^2) and Bjorken- x , thereby enabling the study of phenomena such as nuclear shadowing and gluon saturation. The deployment of high-energy electron beams in interactions with protons and heavy ions facilitate precise measurements of the spatial and momentum distributions of gluons within the target [4], which is crucial for advancing our understanding of quantum chromodynamics (QCD) in dense nuclear environments.

Exclusive photoproduction is a key process for probing the gluon distribution within nuclei. In this process, a virtual photon emitted by an electron coherently interacts with the target, producing a vector meson while leaving the target intact. This interaction serves as a direct probe of the gluon density, as the cross-section is sensitive to the gluon distribution within the target. Specifically, in coherent photoproduction, the virtual photon fluctuates into a quark-antiquark pair, which subsequently scatters elastically from the target through the ex-

change of a color-neutral object, typically a Pomeron, at high energies [5]. Such studies are essential in understanding phenomena such as gluon shadowing, where gluon densities in nuclei are suppressed compared with those in free protons, and in providing compelling evidence for gluon saturation and the formation of color glass condensates [6–9].

To gain insights into the spatial distribution and fluctuations of gluons, measurements of the differential cross section $d\sigma/dt$ are of paramount importance [10]. Momentum transfer t is directly related to the transverse distance between the interacting particles, thereby yielding essential information on the spatial distribution of gluons within the nucleus. In relativistic heavy-ion collisions, significant progress has been made in probing this distribution via $d\sigma/dt$ measurements [11]. Early studies conducted by the STAR experiment at the Relativistic Heavy Ion collider (RHIC) utilized ρ meson photoproduction to reconstruct the spatial distribution of gluons via an inverse Fourier transform of the $d\sigma/dt$ distribution [12]. Further advancements were achieved by the ALICE experiment at the Large Hadron Collider (LHC), which measured $d\sigma/dt$ while accounting for the transverse momentum of the photons [13]. This approach introduced interference effects that facilitated a more detailed analysis of gluon spatial distributions. More recently, STAR [14] reported measurements of ρ meson photoproduction that exploited the linear polarization of photons, which introduced an additional dimension to the analysis, thereby enhancing the sensitivity to spatial anisotropy and gluon density fluctuations within the nucleus.

The accurate determination of the t distribution also necessitates a comprehensive understanding of the transverse momentum distribution of the photons involved in photoproduction. As this transverse momentum distribution cannot be directly measured, it is typically approximated using the Equivalent Photon Approximation (EPA) [15], which inherently involves integration over the impact parameter. However, re-

* This work was supported in part by the National Key Research and Development Program of China under Contract No. 2022YFA1604900 and the National Natural Science Foundation of China (NSFC) under Contract No. 12175223 and 12005220. W. Zha is supported by Anhui Provincial Natural Science Foundation No. 2208085J23 and Youth Innovation Promotion Association of Chinese Academy of Science.

† Corresponding author, Wangmei Zha Address: No. 96 Jinzhai Road, Hefei city, China Tel: +86 551 63607940 Email: first@ustc.edu.cn

62 cent theoretical and experimental studies on photon-photon
 63 collisions in heavy ion collisions have demonstrated that the
 64 photon transverse momentum distribution is highly dependent
 65 on the collision impact parameter [16–21]. This dependence
 66 necessitates a detailed investigation of the parameter
 67 dependence of exclusive photoproduction processes. In both
 68 electron-ion collisions and ultra-peripheral heavy-ion col-
 69 lisions (UPCs), conventional methods, such as using charged-
 70 particle multiplicity to determine the impact parameter, are
 71 not feasible. Recent measurements by the STAR [18], AL-
 72 ICE [22, 23], and CMS [9, 19] experiments have successfully
 73 utilized neutron emission from the Coulomb excitation of nu-
 74 clei to effectively control the “collision centrality” in UPCs.
 75 This progress motivates the adoption of a similar technique
 76 for regulating the impact parameter in electron-ion collisions
 77 specifically by tagging neutrons from Coulomb excitation to
 78 determine the interaction centrality, that is, the impact par-
 79 meter.

80 Determining the probability of Coulomb dissociation (CD)
 81 as a function of the impact parameter in UPCs necessitates
 82 the calculation of the photon flux in spatial coordinates. In
 83 UPCs, the spatial distribution of the photon flux is typically
 84 computed using EPA, which assumes a straight-line trajec-
 85 tory for the ions involved. This assumption is valid when the
 86 motion of colliding ions is not significantly influenced by the
 87 electromagnetic field over the collision duration. However,
 88 in electron-ion collisions at an EIC, the photon flux induced
 89 by the electron cannot be described by the conventional EPA,
 90 as the straight-line approximation breaks down owing to the
 91 substantial deflection of the electron under the electromag-
 92 netic field of the heavy ion. Consequently, a precise deriva-
 93 tion of the spatial distribution of the photon flux induced by
 94 the electron is essential to accurately calculate the CD prob-
 95 ability as a function of the impact parameter in electron-ion
 96 collisions.

97 This study aims to address these challenges by extending
 98 the conventional EPA framework to incorporate the unique
 99 dynamics of electron-induced photon flux in electron-ion col-
 100 lisions. By developing a spatially dependent photon flux dis-
 101 tribution, we aim to establish a more precise relationship
 102 between the transverse momentum distribution of photons
 103 and the impact parameters of the collisions. Within this re-
 104 fined framework, we propose to study the impact par-
 105 meter manipulation in exclusive photoproduction processes in
 106 electron-ion collisions by tagging neutrons from Coulomb ex-
 107 citation. By achieving impact parameter control via neutron
 108 tagging, this study introduces a new methodology for prob-
 109 ing the spatial and momentum structures of gluons in nuclei,
 110 thereby contributing to the experimental design and data anal-
 111 ysis strategies for future electron-ion collision experiments.
 134

II. METHODOLOGY

A. Kinematics of Electron-Proton/Nucleus Scattering

114 To derive the photon flux, we begin by analyzing the kin-
 115 ematics of lowest-order of electron-proton ($e + p$) scattering,

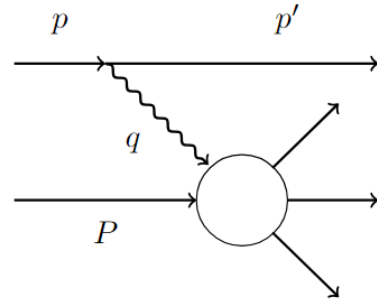


Fig. 1. (Color online) Feynman-like diagram for electron-proton scattering. p and p' are the four-momenta of the electron before and after scattering, respectively. Furthermore, q and P represent the four-momentum of the photon and proton, respectively.

as illustrated in Fig. 1. Although our primary interest lies in electron-nucleus ($e + A$) collisions, the photon flux generated by the electron is essentially the same in both $e + p$ and $e + A$ interactions. Therefore, to ensure both simplicity and generality in the derivation, we perform the analysis within the context of $e + p$ -scattering. Let the z-axis be the direction of motion of the incident electron. The four vector of the incident electron p and that of the scattering electron p' are given by

$$p = (E_e, 0, 0, p_z) \quad (1)$$

and

$$p' = (E'_e, p_x, p_y, p'_z). \quad (2)$$

The four-momentum q of the emitted photons is

$$q = (\omega, -p_x, -p_y, p_\gamma). \quad (3)$$

The four-momentum conservation is as follows:

$$p_z = p'_z + p_\gamma, \quad (4)$$

$$E_e = E'_e + \omega, \quad (5)$$

$$E_e^2 = p_z^2 + m_e^2, \quad (6)$$

$$p_T^2 = E_e'^2 - p_z'^2 - m_e^2 = (E_e - \omega)^2 - (p_z - p_\gamma)^2 - m_e^2, \quad (7)$$

where E_e and E'_e are the energies of the incident and scattering electrons, respectively; m_e is the mass of the electron; p_z and p'_z are the z-components of the momentum of the incident and scattering electrons, respectively; ω and p_T are the energy and transverse momentum of the virtual photon. The momentum of the virtual photon is

$$p_\gamma = p_z - \sqrt{(E_e - \omega)^2 - p_T^2 - m_e^2}. \quad (8)$$

The virtuality of the photon is expressed as

$$q^2 = \omega^2 - p_T^2 - p_\gamma^2 \quad (9)$$

$$= \omega^2 - p_T^2 - \left(p_z - \sqrt{(E_e - \omega)^2 - p_T^2 - m_e^2} \right)^2. \quad (10)$$

136 The virtuality of the photon reaches its minimum and max-158
 137 imum values in two distinct scenarios: when the electron's159
 138 direction remains unchanged after scattering, and when the
 139 electron's direction is reversed following scattering. Then,
 140 q_{\min}^2 and q_{\max}^2 can be written as

$$q_{\min}^2 = 2E_e\omega - 2E_e^2 + 2m_e^2 + 2\sqrt{(E_e^2 - m_e^2)[(E_e - \omega)^2 - m_e^2]},$$

$$q_{\max}^2 = \omega^2 - \left[\sqrt{E_e^2 - m_e^2} + \sqrt{(E_e - \omega)^2 - m_e^2} \right]^2. \quad (11)$$

141 The maximum photon energy is $E_e - m$, which consequently162
 142 results in

$$q_{\max}^2|_{\omega=E_e-m} = q_{\min}^2|_{\omega=E_e-m} = 2m_e^2 - 2E_e m, \quad (12)$$

143 This indicates that the photon flux is zero at $\omega = \omega_{\max}$, which
 144 is consistent with our expectations. For $Q^2 = -q^2 \ll \omega^2$, the
 145 Q_{\min}^2 and Q_{\max}^2 are expressed as

$$Q_{\min}^2 = \frac{m_e^2 \omega^2}{E_e(E_e - \omega)}, \quad (13)$$

$$Q_{\max}^2 = 4E_e(E_e - \omega). \quad (14)$$

B. Photon Flux Derivation

146 Considering the lowest order of QED, the cross-section for
 147 the process shown in Fig. 1 is given by [24]

$$d\sigma_{ep} = \sigma_{\gamma}(\omega)dn, \quad (15)$$

148 $\sigma_{\gamma}(\omega)$ is the absorption cross section for photons with
 149 frequency ω , and dn is the equivalent photon number. Let the
 150 amplitude for virtual photon absorption be represented as M^{μ}
 151 On averaging over the initial spin states and summing across
 152 the final states, the cross section for electron-proton scattering
 153 is given by

$$d\sigma_{ep} = \frac{4\pi\alpha}{(-q^2)} M^{*\nu} M^{\mu} \rho^{\mu\nu} \times \frac{(2\pi)^4 \delta(p + P - p' - k) d\Gamma}{4\sqrt{(pP)^2 - p^2 P^2}} \frac{d^3 p'}{2E'_e(2\pi)^3}, \quad (16)$$

154 where, Γ is the phase space volume and $\rho^{\mu\nu}$ is the density
 155 matrix of the virtual photon produced by an electron that is
 156 given by

$$\rho^{\mu\nu} = \frac{1}{2(-q^2)} \text{Tr} [(\not{p} + m_e) \gamma^{\mu} (\not{p}' + m_e) \gamma^{\nu}] = -\left(g^{\mu\nu} - \frac{q^{\mu} q^{\nu}}{q^2}\right) - \frac{(2p - q)^{\mu} (2p - q)^{\nu}}{q^2}. \quad (17)$$

For a nucleus with a defined charge distribution, rather than a point-like particle, Eq. 17 can be extended to the following:

$$\rho^{\mu\nu} = \frac{1}{2(-q^2)} \text{Tr} [(\not{p} + m) \gamma^{\mu} (\not{p}' + m) \gamma^{\nu}] = -\left(g^{\mu\nu} - \frac{q^{\mu} q^{\nu}}{q^2}\right) C(Q^2) \quad (18)$$

$$- \frac{(2p - q)^{\mu} (2p - q)^{\nu}}{q^2} D(Q^2), \quad (19)$$

where, $C(Q^2) = F_M^2(Q^2)$ and $D(Q^2) = \frac{4m^2 F_E^2 + Q^2 F_M^2}{4m^2 + Q^2}$ and F_M^2 and F_E^2 are the magnetic and electric form factors of the nucleus, respectively. After integration over the phase-space volume, the cross section can be expressed as

$$d\sigma = \frac{\alpha}{4\pi^2 |q^2|} \left[\frac{(qP)^2 - q^2 P^2}{(pP)^2 - p^2 P^2} \right]^{1/2} \times (2\rho^{++} \sigma_T + \rho^{00} \sigma_S) \frac{d^3 p'}{E'_e}, \quad (20)$$

σ_T and σ_S are the cross-sections for transverse and scalar photon absorption, respectively, and σ_S is negligible. The coefficients ρ^{ab} are the elements of the density matrix in the γp -helicity basis, written as

$$2\rho^{++} = \frac{(2pP - qP)^2}{(qP)^2 - q^2 P^2} + 1 + \frac{4m_e^2}{q^2}, \quad \rho^{00} = 2\rho^{++} - \frac{4m_e^2}{q^2} - 2. \quad (21)$$

In the remaining frame of the proton, that is, the target frame, the following relationship holds.

$$\omega = \frac{qP}{m_p}, \quad E_e = \frac{pP}{m_p}, \quad \frac{d^3 p'}{E'_e} = \frac{d\omega d(-q^2) d\varphi}{2\sqrt{E_e^2 - m_e^2}}. \quad (22)$$

Let $Q^2 = -q^2$, where the equivalent photon number is:

$$\frac{d^2 n}{dQ^2 d\omega} = \frac{\alpha}{2\pi Q^2 E_e(E_e - m_e)} \rho^{++} \sqrt{\omega^2 + Q^2} = \frac{\alpha}{4\pi Q^2 E_e(E_e - m_e)} \times \left[\frac{(2E_e - \omega)^2}{\omega^2 + Q^2} + 1 - \frac{4m_e^2}{Q^2} \right] \sqrt{\omega^2 + Q^2}. \quad (23)$$

Here, $\frac{d^2 n}{dQ^2 d\omega}$ can be converted into $\frac{d^2 n}{dp_T d\omega}$ by applying a variable change.

$$dQ^2 d\omega = \begin{vmatrix} \frac{\partial Q^2}{\partial p_T} & \frac{\partial Q^2}{\partial \omega} \\ \frac{\partial \omega}{\partial p_T} & \frac{\partial \omega}{\partial \omega} \end{vmatrix} dp_T d\omega = \frac{2p_z p_T}{\sqrt{(E_e - \omega)^2 - p_T^2 - m_e^2}} dp_T d\omega, \quad (24)$$

$$\frac{d^2 n}{dp_T d\omega} = \frac{2p_z p_T}{\sqrt{(E_e - \omega)^2 - p_T^2 - m_e^2}} \frac{d^2 n}{dQ^2 d\omega}. \quad (25)$$

174 The photon density matrix can be treated as the square of the
 175 photon wave function. Therefore, the equivalent photon num-
 176 ber in the coordinate space can be obtained by performing a
 177 representation transformation in Eq. 25:

$$\frac{d^3 n}{d^2 r d\omega} = \frac{\alpha}{\omega \pi^2} \left(\int_0^{p_{T_{\max}}} \sqrt{\frac{p_T \pi \omega}{2\alpha} \frac{d^2 n}{dp_T d\omega}} J_1(p_T \cdot r) \right)^2, \quad (26)$$

178 $p_{T_{\max}}$ is determined using Q^2 , E_e and ω . Hereafter, we refer
 179 to the method for obtaining the photon flux in this manner as
 180 the lowest-order QED approach.

181 For photoproduction in relativistic heavy-ion collisions,
 182 the photon flux is typically estimated using the conventional
 183 EPA, which was independently derived by Williams [25] and
 184 Weizsäcker [26] in the 1930s. In their derivation, they as-
 185 sumed that the charged particles moved along straight-line
 186 trajectories and obtained the spatial distribution of the electro-
 187 magnetic field by solving the vector potential wave equation.
 188 The spatial distribution of the equivalent photon number was
 189 subsequently derived based on the relationship between the
 190 energy flux density and equivalent photon number. This ap-
 191 proach provides an effective way to describe the photon flux
 192 distribution, which can be expressed as

$$\begin{aligned} n(\omega, \vec{x}_\perp) &= \frac{1}{\pi\omega} \left| \vec{E}_\perp(\omega, \vec{x}_\perp) \right|^2 \\ &= \frac{4Z^2\alpha}{\omega} \left| \int \frac{d^2 \vec{k}_\perp}{(2\pi)^2} \vec{k}_\perp \frac{F\left(\vec{k}_\perp^2 + \left(\frac{\omega}{\gamma}\right)^2\right)}{\vec{k}_\perp^2 + \left(\frac{\omega}{\gamma}\right)^2} e^{i\vec{x}_\perp \cdot \vec{k}_\perp} \right|^2 \\ &= \frac{Z^2\alpha}{\pi^2\omega} \left| \int_0^\infty dk_\perp k_\perp^2 \frac{F\left(k_\perp^2 + \left(\frac{\omega}{\gamma}\right)^2\right)}{k_\perp^2 + \left(\frac{\omega}{\gamma}\right)^2} J_1(x_\perp k_\perp) \right|^2, \end{aligned} \quad (27)$$

193 where Z denotes the charge number of the charged particle, γ
 194 represents the Lorentz factor of the charged particle, ω is the
 195 photon energy. For a point-like particle, the photon flux is

$$n_{\text{pt}}(\omega, x_\perp) = \frac{Z^2 \alpha_{QED} \omega}{\pi^2 \gamma^2} \left[K_1 \left(\frac{\omega x_\perp}{\gamma} \right) \right]^2. \quad (28)$$

196 C. Coulomb Dissociation in Electron-Ion Collisions

197 Analogous to the Coulomb excitation process in relativis-
 198 tic heavy-ion collisions, Coulomb excitation in electron-ion
 199 collisions can be factorized into two distinct components: the
 200 emission of virtual photons by electrons and the correspond-
 201 ing photon absorption cross-section of the nucleus. The vir-
 202 tual photons emitted by electrons can be estimated using the
 203 framework described in the previous subsection.

204 The lowest-order probability that a nucleus is excited to a
 205 state that subsequently emits at least one neutron (denoted as
 206 Xn) can be expressed as [27]

$$m_{Xn}(b) = \int d\omega n(\omega, b) \sigma_{Xn, \gamma A \rightarrow A^*}(\omega), \quad (29)$$

207 where $n(\omega, b)$ represents the photon flux at a given impact
 208 parameter b and $\sigma_{Xn, \gamma A \rightarrow A^*}(\omega)$ is the photoexcitation cross
 209 section for an incident photon with energy ω obtained from
 210 experimental data [28–32].

211 Notably, under specific conditions, such as very small im-
 212 pact parameters and extremely high beam energies, the value
 213 of m_{Xn} could exceed 1, implying that the excitation prob-
 214 ability would lose its probabilistic interpretation. Although
 215 such conditions are improbable in current or near-future fa-
 216 cilities, it is beneficial to address this scenario for the sake
 217 of completeness. To maintain a valid probabilistic interpre-
 218 tation, $m_{Xn}(b)$ is treated as the mean number of photons ab-
 219 sorbed by the nucleus and we assume that the photon multi-
 220 plicity follows a Poisson distribution [33, 34]. In this context,
 221 the probability of absorbing zero photons (i.e., zero neutron
 222 emission) is given by

$$P^{(0)}(b) = e^{-m_{Xn}(b)}, \quad (30)$$

223 whereas, the probability of exactly absorbing N photons is:

$$P^{(N)}(b) = \frac{m_{Xn}^N(b)}{N!} e^{-m_{Xn}(b)}. \quad (31)$$

224 The normalized probability density for the absorption of
 225 one photon with energy E_1 can be expressed as

$$p^{(1)}(E_1, b) = \frac{n(E_1, b) \sigma_{\gamma A \rightarrow A^*(E_1)}}{m_{Xn}(b)}, \quad (32)$$

226 and the probability density for absorbing N photons with en-
 227 ergies E_1, E_2, \dots, E_N is:

$$p^{(N)}(E_1, E_2, \dots, E_N, b) = \frac{\prod_{i=1}^N n(E_i, b) \sigma_{\gamma A \rightarrow A^*(E_i)}}{m_{Xn}(b)}. \quad (33)$$

228 For a specific electromagnetic dissociation channel involv-
 229 ing the emission of i neutrons, the probability density of an
 230 N -photon absorption process can be evaluated as

$$\begin{aligned} P_i^{(N)}(b) &= \int \dots \int dE_1 \dots dE_N \\ &\times P^{(N)}(b) p^{(N)}(E_1, \dots, E_N, b) f_i(E_1, \dots, E_N), \end{aligned} \quad (34)$$

231 where, $f_i(E_1, \dots, E_N)$ represents the branching ratio of
 232 a specific channel with i emitted neutrons. We assume
 233 that simultaneous absorption of multiple photons is al-
 234 lowed, leading to a simplified form of the branching ratio,
 235 $f_i(E_1, \dots, E_N) = f_i\left(\sum_{k=1}^N E_k\right)$. The values of f_i for
 236 different neutron emission channels were extracted from the
 237 n_{O}^{on} model, as described in Ref. [35].

238 Finally, the total probability of emission of i neutrons is
 239 given by

$$P_{\text{in}}(b) = \sum_{k=1}^{\infty} P_i^{(k)}(b). \quad (35)$$

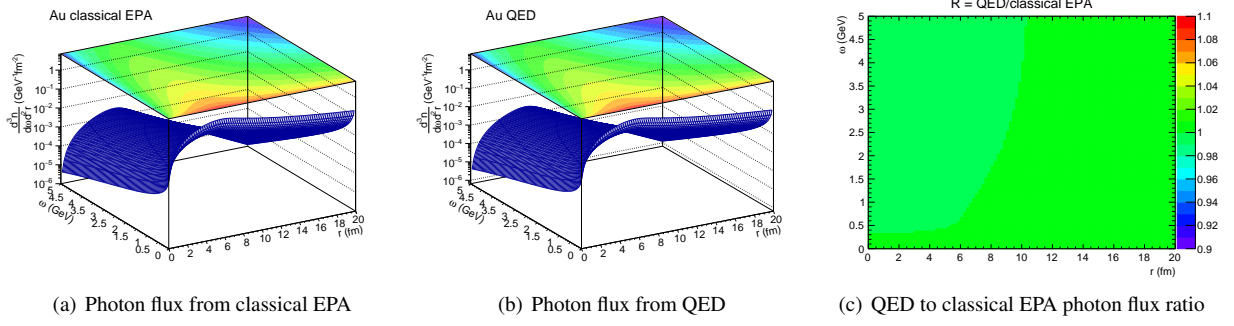


Fig. 2. (Color online) Comparison of the photon flux distribution induced by a Au nucleus with $E = 100$ GeV per nucleon, as calculated using the conventional EPA model (panel a) and the QED derivation (panel b), as well as the ratio of the QED results to the classical EPA results (panel c).

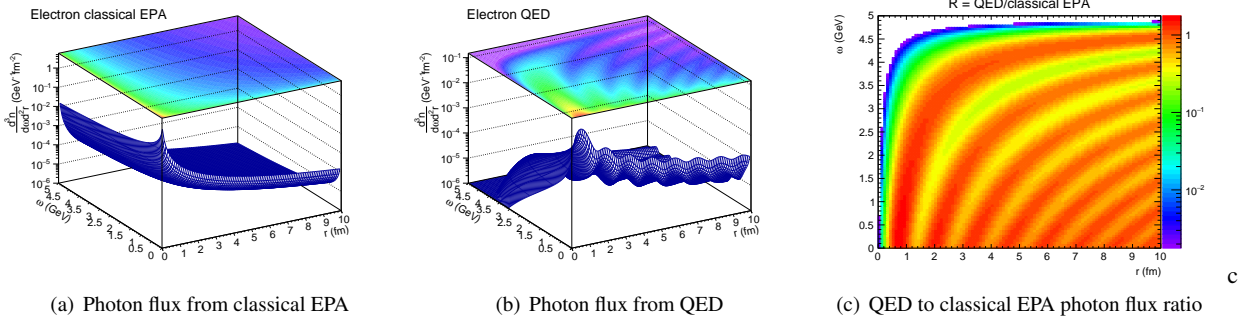


Fig. 3. (Color online) Comparison of the photon flux distribution induced by an electron with $E = 5$ GeV, as calculated using the conventional EPA model (panel a) and the QED derivation (panel b), along with the ratio of the QED results to the classical EPA results (panel c).

242 D. Vector Meson Photoproduction in Electron-Ion Collisions 256

243 The vector meson photoproduction in electron-ion colli-258
 244 sions can be estimated in a manner similar to Coulomb ex-259
 245 citation calculations. The primary difference lies in replacing260
 246 the photon absorption cross section of the nucleus with the261
 247 $\gamma A \rightarrow VA$ cross section. Specifically, the scattering am-262
 248 plitude $\Gamma_{\gamma A \rightarrow VA}$, including the shadowing effect, can be derived263
 249 using the Glauber model [36] combined with the vector me-264
 250 son dominance (VMD) approach [37]:

$$\Gamma_{\gamma A \rightarrow VA}(\vec{x}_\perp) = \frac{f_{\gamma N \rightarrow VN}(0)}{\sigma_{VN}} \times 264 \\ 265 2 \left[1 - \exp \left(-\frac{\sigma_{VN}}{2} T'(\vec{x}_\perp) \right) \right], \quad (36) 266$$

267 where, $f_{\gamma N \rightarrow VN}(0)$ is the forward scattering amplitude for268
 269 $\gamma + N \rightarrow V + N$ and σ_{VN} represents the total vector meson-nu-270
 271 cleon (VN) cross-section. The modified nuclear thickness272
 273 function $T'(\vec{x}_\perp)$ that considers the coherence length effect is274
 275 given by

$$T'(\vec{x}_\perp) = \int_{-\infty}^{+\infty} \rho \left(\sqrt{\vec{x}_\perp^2 + z^2} \right) e^{iq_L z} dz, \quad q_L = \frac{M_V e^y}{2\gamma_c}, \quad (37)$$

where, q_L denotes the longitudinal momentum transfer required to produce a real vector meson, M_V is the vector meson mass, and γ_c is the Lorentz factor of the nucleus.

Considering the impact of the photon's virtuality on the photon-nucleon scattering cross-section, the equivalent vector meson flux is introduced as

$$\frac{d^2V}{d\omega dQ^2} = \left(\frac{M_V^2}{M_V^2 + Q^2} \right)^n \frac{d^2n}{d\omega dQ^2}, \quad (38)$$

where $\left(\frac{M_V^2}{M_V^2 + Q^2} \right)^n$ represents the suppression factor associated with the transition amplitude from the virtual photon fluctuation to the corresponding vector meson, and n is determined by fitting the experimental data [38, 39]. The equivalent vector meson flux in the coordinate space $\frac{d^3n}{d^2r d\omega}$ can be obtained using the method outlined in the previous section.

The amplitude distribution for the vector meson photoproduction process is given by

$$A(b, \vec{x}_\perp) = \Gamma_{\gamma A \rightarrow VA}(\vec{r}_1) \sqrt{n(\omega, \vec{r}_2)}, \quad (39)$$

where $\vec{r}_2 - \vec{r}_1 = \vec{b}$ and $\frac{\vec{b}}{2} + \vec{r}_1 = \vec{x}_\perp$. The production amplitude in momentum space can be obtained by applying a Fourier transformation to the amplitude in the coordinate representation:

$$\vec{A}(\vec{p}_\perp, b) = \frac{1}{2\pi} \int d^2x_\perp \vec{A}(\vec{x}_\perp, b) e^{i\vec{p}_\perp \cdot \vec{x}_\perp}. \quad (40)$$

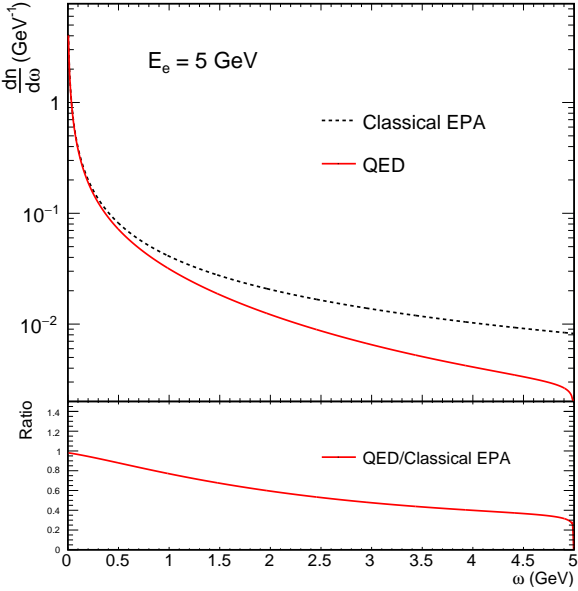


Fig. 4. (Color online) Upper panel: The $\frac{d\sigma}{d\omega}$ distribution calculated from the classical EPA model (black line) and the QED model (red line). Lower panel: The ratio of the QED results to the classical EPA results.

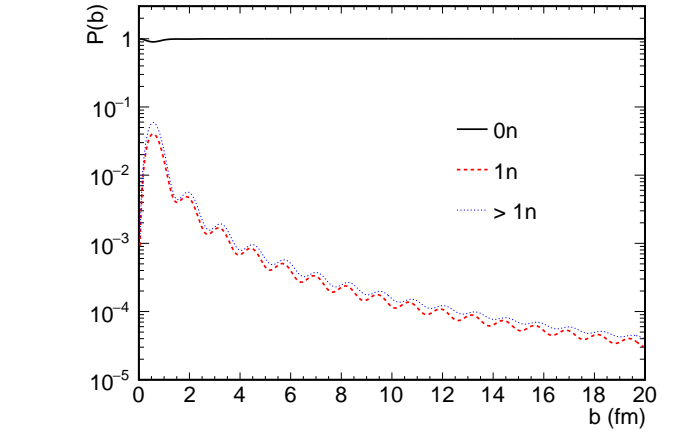


Fig. 5. (Color online) Nucleus break-up probability of Au-197 as a function of impact parameter in e+Au collision at EIC energy (18×100 GeV) for different number of neutron emission. Black line: “0n” mode. Red line: “1n” mode. Blue line: “>1n” mode.

of the Au nucleus, and a subsequent decrease as the photon energy ω increases. Furthermore, the ratio between the QED and classical EPA results remains close to unity, indicating that the classical EPA model provides an accurate approximation of the photon flux for UPCs and is effectively equivalent to the QED-derived expression under these assumptions.

However, the use of Eq. 27 becomes problematic in the context of electron-ion collisions. This is primarily because the energy of an electron is significantly lower than that of a heavy ion, which renders the straight-line approximation invalid. Furthermore, direct application of Eq. 27 does not constrain the photon energy from exceeding the energy of the charged particle, which is physically incorrect. To illustrate this limitation, we compare the photon flux distributions calculated using the classical EPA and QED models for an electron with an energy of 5 GeV. Figure 3 presents the 2D photon flux distribution and the ratio of the QED to classical EPA results. The comparison clearly demonstrates a substantial difference between the two models, with the QED-derived flux showing distinct fluctuations and tending towards zero as the photon energy approaches the electron energy. This behavior underscores the inadequacy of the classical EPA model in describing the photon flux for electron-ion collisions.

Figure 4 provides a further comparison of the photon energy distributions obtained using the classical EPA and QED models. The photon flux calculated using the QED model closely follows the classical EPA prediction at low photon energies but rapidly approaches zero as the photon energy approaches the total energy of the electron. In contrast, the photon flux calculated using the classical EPA model decreases smoothly without reaching zero. This discrepancy further underscores the limitations of the classical EPA model for electron-ion collisions and demonstrates that the photon flux distribution derived from the QED model is more suitable for accurately describing these processes. Consequently, the QED approach offers a more reliable framework for calcu-

300

301

302

303

304

305

306

307

308

309

310

311

312

313

314

315

316

317

318

319

320

321

322

323

324

325

326

327

328

329

330

331

332

333

334

335

336

337

338

339

340

341

342

343

344

345

346

347

348

349

350

351

352

353

354

355

356

357

358

359

360

361

362

363

364

365

366

367

368

369

370

371

372

373

374

375

376

377

378

379

380

381

382

383

384

385

386

387

388

389

390

391

392

393

394

395

396

397

398

399

400

401

402

403

404

405

406

407

408

409

410

411

412

413

414

415

416

417

418

419

420

421

422

423

424

425

426

427

428

429

430

431

432

433

434

435

436

437

438

439

440

441

442

443

444

445

446

447

448

449

450

451

452

453

454

455

456

457

458

459

460

461

462

463

464

465

466

467

468

469

470

471

472

473

474

475

476

477

478

479

480

481

482

483

484

485

486

487

488

489

490

491

492

493

494

495

496

497

498

499

500

501

502

503

504

505

506

507

508

509

510

511

512

513

514

515

516

517

518

519

520

521

522

523

524

525

526

527

528

529

530

531

532

533

534

535

536

537

538

539

540

541

542

543

544

545

546

547

548

549

550

551

552

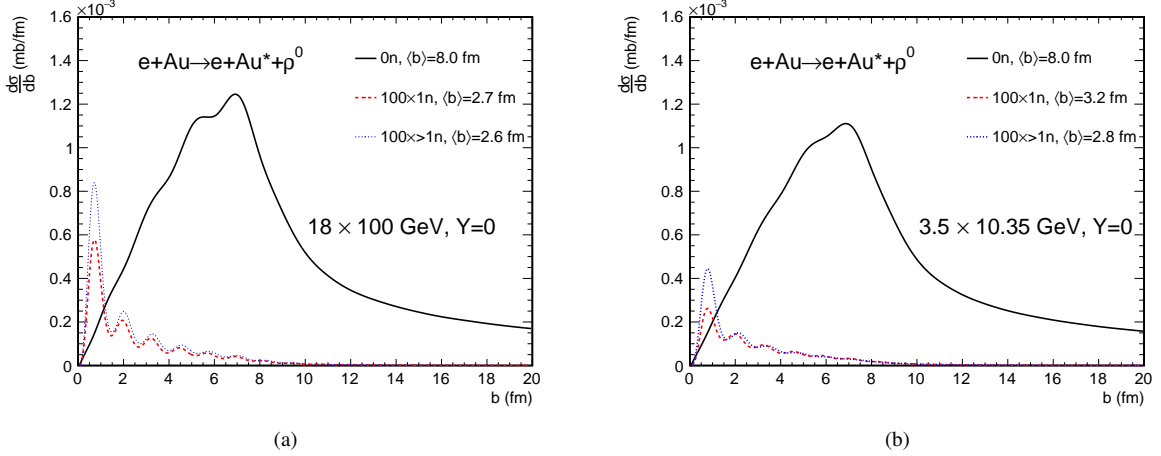


Fig. 6. (Color online) The $\frac{d\sigma}{db}$ for ρ^0 photoproduction at EIC (a) and EicC (b) energy. Black line: “0n” mode. Red line: “1n” mode. Blue line: “>1n” mode. The results of “1n” and “>1n” have been multiplied by 100.

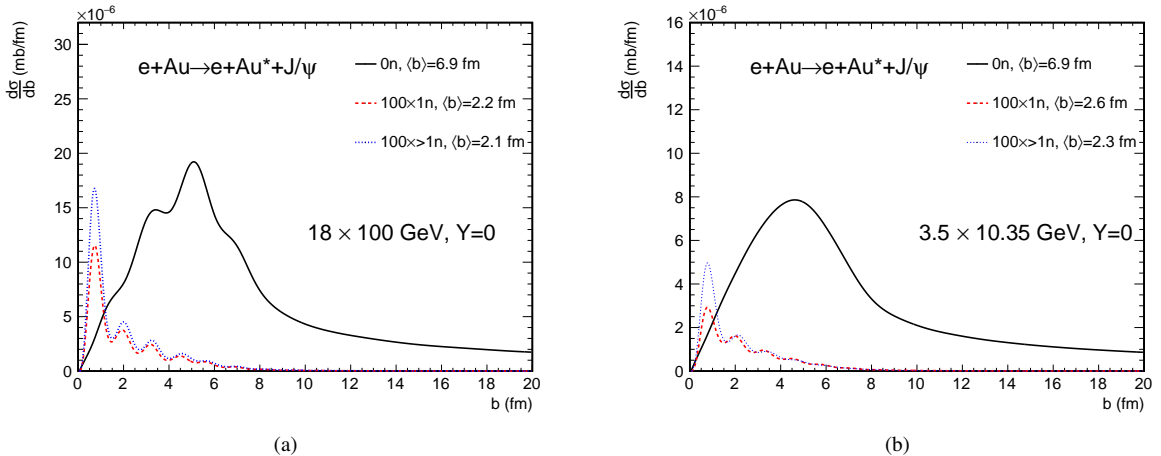


Fig. 7. (Color online) The $\frac{d\sigma}{db}$ for J/ψ photoproduction at EIC (a) and EicC (b) energy. Black line: “0n” mode. Red line: “1n” mode. Blue line: “>1n” mode. The results of “1n” and “>1n” have been multiplied by 100.

lating the impact parameter dependence of photoproduction processes in electron-ion collisions.

The lowest-order QED-derived photon flux enables accurate evaluation of the Coulomb excitation of a nucleus during electron-ion collisions. As an illustrative example, we consider $e + Au$ collisions at the EIC energies, specifically at 18×100 GeV per nucleon. The corresponding $P_{in}(b)$ -distribution, representing the dissociation probability as a function of the impact parameter, is shown in Fig. 5. The dissociation probability, characterized by neutron emission, exhibits a rapid decrease with increasing impact parameter. Notably, the probability distribution exhibits an oscillatory pattern, which can be attributed to the wave nature of the photons emitted by the electrons, resulting in interference effects. Dissociation processes involving a higher number of emitted neutrons are more probable at smaller impact parameters, indicating stronger electromagnetic interactions in more cen-

tral collisions. This characteristic offers a practical method for determining the impact parameter in electron-ion interactions by counting the number of emitted neutrons detected using a zero-degree calorimeter (ZDC). The rapidity distribution of the emitted neutrons was studied at the EIC energy using a DPMJET generator [40], providing valuable insights for designing the ZDC for the EIC. The correlation between neutron emission and the impact parameter enables the categorization of the collision events based on their geometric overlap, facilitating a more precise study of photonuclear interaction dynamics in electron-ion collisions.

Furthermore, the different photoproduction processes, even those with the same neutron tagging, exhibit variations in impact parameter distributions. This is because the photon energies involved in different processes vary, thereby impacting the spatial distribution of photons relative to electrons. Unlike hadronic heavy-ion collisions, where centrality is defined

368 by a fixed impact parameter range, the impact parameter de-401
 369 termination in electron-ion collisions via neutron tagging de-402
 370 pends on the specific photoproduction process under consid-403
 371 eration. Therefore, this must be evaluated on a case-by-case404
 372 basis. To illustrate this, we present calculations for coherent405
 373 ρ^0 and J/ψ photoproduction accompanied by different neu-406
 374 tron tagging at the EIC and EicC energies. 407

375 Figure 6 presents the $d\sigma/db$ distributions for coherent ρ^0 408
 376 photoproduction at the EIC and EicC energies, with different409
 377 line types and colors representing distinct neutron emission410
 378 modes. The average impact parameter for the “0n” mode is411
 379 significantly larger than that for the “1n” and “>1n” (at least412
 380 two neutrons) modes. This is because neutron excitation re-413
 381 quires additional photons, which reduces the average impact414
 382 parameter. The distinct variation in the impact parameters415
 383 across neutron emission modes demonstrates the feasibility of416
 384 determining the impact parameter of electron-ion collisions417
 385 by tagging neutrons from Coulomb excitation. Furthermore,418
 386 the cross section exhibits fluctuations with respect to the im-419
 387 pact parameter, a phenomenon that arises from the oscillatory420
 388 behavior of the J_1 Bessel function in the coordinate distribu-421
 389 tion of the photon flux, as described by Eq. 26. A compari-422
 390 son of the results at the EIC and EicC energies indicates that423
 391 variations in the center-of-mass collision energy have negli-424
 392 gible effect on the average impact parameter, indicating that the425
 393 proposed method is effective across different collision energy426
 394 regimes. 427

395 Figure 7 illustrates the $d\sigma/db$ distributions for coherent426
 396 J/ψ photoproduction at EIC and EicC energies. Similar to427
 397 the ρ^0 case, the average impact parameter for the 0n mode is428
 398 much larger than those for the other neutron emission modes.429
 399 In addition, the average impact parameter $\langle b \rangle$ for J/ψ is430
 400 typically smaller than that for ρ^0 in the corresponding neu-431

401 tron emission modes. This behavior can be attributed to the
 402 larger mass of J/ψ compared with ρ^0 , which corresponds to
 403 a higher photon energy. In addition, this results in a larger
 404 cross-sectional ratio $\sigma_{>1n}/\sigma_{0n}$ of J/ψ than for ρ^0 . Con-
 405 sequently, the photon is closer to the electron, resulting in a
 406 reduced average impact parameter. The sensitive dependence
 407 of the average impact parameter on neutron emission via
 408 Coulomb excitation observed across different vector mesons
 409 further underscores the effectiveness of this method for de-
 410 termining the impact parameter in experimental electron-ion
 411 collisions. 412

IV. SUMMARY

We investigated the feasibility of employing neutron tagging, resulting from the Coulomb excitation of nuclei, as a precise method to ascertain the impact parameters of exclusive photoproduction events in electron-ion collisions. By developing an equivalent photon approximation for electrons, this study integrated a photon flux distribution in coordinate space, thereby validating the relationship between the distribution of the photon’s transverse momentum and the impact parameters of the collisions. The differential cross-section for the Coulomb excitation of nuclei was calculated by leveraging the spatial data of the photon flux. Our calculations indicate that the presence or absence of neutron excitation in the photoproduction process can markedly shift the distributions of impact parameters, thereby offering a reliable technique for controlling the impact parameter in electron-ion collision experiments. This study provides essential methodologies and insights for examining the dependence of exclusive photoproduction processes on impact parameters, yielding novel perspectives for the design of experiments and data analysis.

432 [1] Z. Ji et al., Lambda polarization at the Electron-ion collider in433
 434 China. Nucl. Sci. Tech. **34**, 155 (2023). DOI:10.1007/s41365-454
 435 023-01317-w 455

436 [2] A. Accardi et al., Electron Ion Collider: The Next QCD Fron-456
 437 tier: Understanding the glue that binds us all. Eur. Phys. J. A **457**
 438 **52**, 268 (2016). DOI: 10.1140/epja/i2016-16268-9 458

439 [3] D.P. Anderle et al., Electron-ion collider in China. Front. Phys.
 440 **16**, 64701 (2021). DOI: 10.1007/s11467-021-1062-0 460

441 [4] E. Iancu and R. Venugopalan, The Color glass condensate and461
 442 high-energy scattering in QCD. in Quark-gluon plasma **4**, 249462
 443 (2003). DOI : 10.1142/9789812795533_0005 463

444 [5] J. Bartels, K.J. Golec-Biernat, and K. Peters, On the dipole pic-464
 445 ture in the nonforward direction. Acta Phys. Polon. B **34**, 3051465
 446 (2003).arXiv:hep-ph/0301192. 466

447 [6] S.P. Jones et al., Probes of the small x gluon via exclusive J/ψ 467
 448 and Υ production at HERA and the LHC. JHEP **11**, 085 (2013).468
 449 DOI: 10.1007/JHEP11(2013)085 469

450 [7] D.Yu. Ivanov et al., Exclusive photoproduction of a heavy470
 451 vector meson in QCD. Eur. Phys. J. C **34**, 297 (2004). DOI:471
 452 10.1140/epjc/s2004-01712-x [Erratum: Eur. Phys. J. C **75**, 75472
 453 (2015)] 473

454 [8] X. Wang et al., Exclusive charmonium production at the455
 456 electron-ion collider in China. Eur. Phys. J. C **84**, 684 (2024).
 457 DOI: 10.1140/epjc/s10052-024-13033-9

458 [9] A. Tumasyan et al., [CMS Collaboration], Probing Small
 459 Bjorken-x Nuclear Gluonic Structure via Coherent J/ψ Photoproduction in Ultraperipheral Pb-Pb Collisions at $\sqrt{s_{NN}} =$
 460 5.02 TeV. Phys. Rev. Lett. **131**, 262301 (2023). DOI:
 461 10.1103/PhysRevLett.131.262301

462 [10] T. Toll and T. Ullrich, Exclusive diffractive processes in
 463 electron-ion collisions. Phys. Rev. C **87**, 024913 (2013). DOI:
 464 10.1103/PhysRevC.87.024913

465 [11] S. R. Klein and H. Mäntysaari, Imaging the nucleus with
 466 high-energy photons. Nat. Rev. Phys. **1**, 662 (2019). DOI:
 467 10.1038/s42254-019-0107-6

468 [12] L. Adamczyk et al., (STAR Collaboration), Coherent diffrac-469
 470 tive photoproduction of ρ^0 mesons on gold nuclei at 200
 471 GeV/nucleon-pair at the Relativistic Heavy Ion Collider. Phys.
 472 Rev. C **96**, 054904 (2017). DOI: 10.1103/Phys-
 473 RevC.96.054904

474 [13] S. Acharya et al., (ALICE Collaboration), First measure-
 475 ment of the $|t|$ -dependence of coherent J/ψ photonuclear
 476 production. Phys. Lett. B **817**, 136280 (2021). DOI:

475 [10.1016/j.physletb.2021.136280] 523

476 [14] M. Abdallah et al., (STAR Collaboration), Tomography of ul-524
477 trarelativistic nuclei with polarized photon-gluon collisions.525
478 Sci. Adv. **9**, 1 (2023). DOI: [10.1126/sciadv.abq3903](https://doi.org/10.1126/sciadv.abq3903) 526

479 [15] E. Fermi, On the Theory of the impact between atoms and527
480 electrically charged particles. Z. Phys. **29**, 315 (1924). DOI: [10.1007/BF03184853](https://doi.org/10.1007/BF03184853) 528

481 [16] W. Zha et al., Initial transverse-momentum broaden-530
482 ing of Breit-Wheeler process in relativistic heavy-ion531
483 collisions. Phys. Lett. B **800**, 135089 (2020). DOI: [10.1016/j.physletb.2019.135089](https://doi.org/10.1016/j.physletb.2019.135089) 533

484 [17] M. Klusek-Gawenda, W. Schäfer, and A. Szczurek, Central-534
485 ity dependence of dilepton production via $\gamma\gamma$ processes from535
486 Wigner distributions of photons in nuclei. Phys. Lett. B **814**, 536
487 136114 (2021). DOI: [10.1016/j.physletb.2021.136114](https://doi.org/10.1016/j.physletb.2021.136114) 537

488 [18] J. Adam et al., [STAR Collaboration], Measurement of e^+e^- 538
489 Momentum and Angular Distributions from Linearly Polarized539
490 Photon Collisions. Phys. Rev. Lett. **127**, 052302 (2021). 540

491 [19] A. M. Sirunyan et al., [CMS Collaboration], Observation541
492 of Forward Neutron Multiplicity Dependence of Dimuon542
493 Acoplanarity in Ultraperipheral Pb-Pb Collisions at $\sqrt{s_{NN}} =$ 543
494 5.02 TeV. Phys. Rev. Lett. **127**, 122001 (2021). DOI: [10.1103/PhysRevLett.127.122001](https://doi.org/10.1103/PhysRevLett.127.122001) 544

495 [20] J. Chen et al., Properties of the QCD Matter – An Experimental545
496 Review of Selected Results from RHIC BES Program. DOI: [10.48550/arXiv.2407.02935](https://doi.org/10.48550/arXiv.2407.02935) 548

497 [21] J. Zhao et al., Electromagnetic fields in ultra-peripheral rel-549
500 ativistic heavy-ion collisions. Nucl. Sci. Tech. **35**, 20 (2024) 550
501 DOI: [10.1007/s41365-024-01374-9](https://doi.org/10.1007/s41365-024-01374-9). 551

502 [22] S. Acharya et al., [ALICE Collaboration], Measurements552
503 of the impact-parameter dependent azimuthal anisotropy553
504 in coherent ρ^0 photoproduction in Pb-Pb collisions at554
505 $\sqrt{s_{NN}} = 5.02$ TeV. Phys. Lett. B **858**, 139017 (2024). DOI: [10.1016/j.physletb.2024.139017](https://doi.org/10.1016/j.physletb.2024.139017) 556

506 [23] S. Acharya et al., [ALICE Collaboration], Energy dependence557
507 of coherent photonuclear production of J/ψ mesons in ultra-558
508 peripheral Pb-Pb collisions at $\sqrt{s_{NN}} = 5.02$ TeV. JHEP **10**, 119 559
509 (2023). DOI: [10.1007/JHEP10\(2023\)119](https://doi.org/10.1007/JHEP10(2023)119) 560

510 [24] V.M. Budnev et al., The Two photon particle production mech-561
511 anism. Physical problems. Applications. Equivalent photon ap-562
512 proximation. Phys. Rept. **15**, 181 (1975). DOI: [10.1016/0370-1573\(75\)90009-5](https://doi.org/10.1016/0370-1573(75)90009-5) 564

513 [25] E.J. Williams, Sowie eine im Erscheinen begrifene Fortsetzung565
514 dieser Arbeit. Proceedings of the Royal Society of London Se-566
515 ries A **139**, 163 (1933). 567

516 [26] C.F. von Weizsäcker, Radiation emitted in collisions of568
517 very fast electrons. Z. Phys. **88**, 612 (1934). DOI: [10.1007/BF01333110](https://doi.org/10.1007/BF01333110) 569

518 [27] A.J. Baltz, M.J. Rhoades-Brown, and J. Weneser, Heavy 570
519 ion partial beam lifetimes due to Coulomb induced pro-520
521 cesses. Phys. Rev. E **54**, 4233 (1996). DOI: [10.1103/PhysRevE.54.4233](https://doi.org/10.1103/PhysRevE.54.4233)

522 [28] A. Veyssiére et al., Photoneutron cross sections of 208Pb and 523
523 197Au. Nucl. Phys. A **159**, 561 (1970). DOI: [10.1016/0375-9474\(70\)90727-X](https://doi.org/10.1016/0375-9474(70)90727-X)

524 [29] A. Lepretre et al., Measurements of the Total Photonuclear 525
525 Cross-sections From 30-MeV to 140-MeV for SN, Ce, Ta, 526
526 Pb and U Nuclei. Nucl. Phys. A **367**, 237 (1981). DOI: 527
527 [10.1016/0375-9474\(81\)90516-9](https://doi.org/10.1016/0375-9474(81)90516-9)

528 [30] P. Carlos et al., Total photonuclear absorption cross-section for 529
529 Pb and for heavy nuclei in the delta resonance region. Nucl. 530
530 Phys. A **431**, 573 (1984). DOI: [10.1016/0375-9474\(84\)90269-0](https://doi.org/10.1016/0375-9474(84)90269-0)

531 [31] D.O. Caldwell et al., Total Hadronic Photoabsorption Cross- 532
532 Sections on Hydrogen and Complex Nuclei from 4-GeV to 533
533 18-GeV. Phys. Rev. D **7**, 1362 (1973). DOI: [10.1103/PhysRevD.7.1362](https://doi.org/10.1103/PhysRevD.7.1362)

534 [32] T.A. Armstrong et al., The total photon deuteron hadronic 535
535 cross-section in the energy range 0.265-4.215 GeV. Nucl. Phys. 536
536 B **41**, 445 (1972). DOI: [10.1016/0550-3213\(72\)90403-8](https://doi.org/10.1016/0550-3213(72)90403-8)

537 [33] I.A. Pshenichnov et al., Mutual heavy ion dissociation in 538
538 peripheral collisions at ultrarelativistic energies. Phys. Rev. C **64**, 539
539 024903 (2001). DOI: [10.1103/PhysRevC.64.024903](https://doi.org/10.1103/PhysRevC.64.024903)

540 [34] I.A. Pshenichnov et al., Particle emission following Coulomb 541
541 excitation in ultrarelativistic heavy ion collisions. Phys. Rev. C **60**, 542
542 044901 (1999). DOI: [10.1103/PhysRevC.60.044901](https://doi.org/10.1103/PhysRevC.60.044901)

543 [35] M. Broz et al., A generator of forward neutrons for ultra- 544
544 peripheral collisions: n_0^0 . Comput. Phys. Commun. **253**, 545
545 107181 (2020). DOI: [10.1016/j.cpc.2020.107181](https://doi.org/10.1016/j.cpc.2020.107181)

546 [36] M.L. Miller et al., Glauber modeling in high energy nuclear 547
547 collisions. Ann. Rev. Nucl. Part. Sci. **57**, 205 (2007). DOI: 548
548 [10.1146/annurev.nucl.57.090506.123020](https://doi.org/10.1146/annurev.nucl.57.090506.123020)

549 [37] T.H. Bauer et al., The Hadronic Properties of the Photon in 550
550 High-Energy Interactions. Rev. Mod. Phys. **50**, 261 (1978). 551
551 DOI: [10.1103/RevModPhys.50.261](https://doi.org/10.1103/RevModPhys.50.261). Note: Erratum: Rev. 552
552 Mod. Phys. 51, 407 (1979)

553 [38] C. Adloff et al., [H1 Collaboration], Elastic electroproduction 554
554 of rho mesons at HERA. Eur. Phys. J. C **13**, 371 (2000). DOI: 555
555 [10.1007/s100520050703](https://doi.org/10.1007/s100520050703)

556 [39] F.D. Aaron et al., [H1 Collaboration], Diffractive Electropro- 557
557 duction of ρ and ϕ Mesons at HERA. JHEP **05**, 032 (2010). 558
558 DOI: [10.1007/JHEP05\(2010\)032](https://doi.org/10.1007/JHEP05(2010)032)

559 [40] L. Zheng, E.C. Aschenauer and J.H. Lee, Determination of 560
560 electron-nucleus collision geometry with forward neutrons. 561
561 Eur. Phys. J. A **50**, 189 (2014). DOI: [10.1140/epja/i2014-14189-3](https://doi.org/10.1140/epja/i2014-14189-3)